Noname manuscript No.
(will be inserted by the editor)

Symmetry Prior for Epipolar Consistency

Alexander Preuhs · Andreas Maier · Michael Manhart · Markus Kowarschik · Elisabeth Hoppe · Javad Fotouhi · Nassir Navab · Mathias Unberath

Received: date / Accepted: date

Abstract
Purpose: For a perfectly plane symmetric object we can find two views — mirrored at the plane of symmetry — that will yield the exact same image of that object. In consequence, having one image of a plane symmetric object and a calibrated camera, we automatically have a second, virtual image of that object if the 3-D location of the symmetry plane is known.
Methods: We propose a method for estimating the symmetry plane from a set of projection images as the solution of a consistency maximization based on epipolar consistency. With the known symmetry plane, we can exploit symmetry to estimate in-plane motion by introducing the X-trajectory that can be acquired with a conventional short scan trajectory by simply tilting the acquisition plane relative to the plane of symmetry.
Results: We inspect the symmetry plane estimation on a real scan of an anthropomorphic human head phantom and show the robustness using a synthetic dataset. Further, we demonstrate the advantage of the proposed method for estimating in-plane motion using the acquired projection data.
Conclusion: Symmetry breakers in the human body are widely used for the detection of tumors or strokes. We provide a fast estimation of the symmetry plane, robust to outliers, by computing it directly from a set of projections. Further, by coupling the symmetry prior with epipolar consistency we overcome inherent limitations in the estimation of in-plane motion.

Keywords symmetry, consistency conditions, cone-beam CT, motion compensation, data completeness, tomographic reconstruction

Alexander Preuhs · Elisabeth Hoppe · Andreas Maier
Pattern Recognition Lab, Friedrich-Alexander Universität Erlangen-Nürnberg, Germany
E-mail: alexander.preuhs@fau.de

Michael Manhart · Markus Kowarschik
Siemens Healthcare GmbH, Forchheim, Germany

Mathias Unberath · Javad Fotouhi · Nassir Navab
Department of Computer Science, Johns Hopkins University, Baltimore, MD, USA

1 Introduction

Symmetry is a powerful concept with applications ranging from art to physics and mathematics [9,8]. This manuscript is concerned with symmetry in computer vision where we consider a theoretically sound yet surprisingly little known property of symmetric objects: when imaging a symmetric object using a calibrated camera, knowledge of the 3-D symmetry plane yields a second, virtual camera that corresponds to a mirrored version of the image seen by the true camera. This circumstance enables metric 3-D stereo reconstruction of symmetric objects using a single calibrated camera [27,10,11].

For the first time, Preuhs *et al.* [23] have demonstrated that the above property naturally extends to transmission imaging, *i. e.* X-ray fluoroscopy, and devised image-based algorithms that exploit this circumstance to estimate intra-scan motion in circular C-arm cone-beam computed tomography (CBCT). In CBCT imaging, all camera positions are calibrated suggesting that a virtual source trajectory becomes available once the 3-D symmetry plane is known. This paper is an extension of our prior work in Preuhs *et al.* [23] that provided a proof of concept study.

Several methods have investigated the estimation of a bilateral symmetry, either by finding a symmetry plane in 3-D or the symmetry axis on 2-D images. A majority of these approaches formulate a similarity function between an original image, and the mirrored version of that image [15,33,20,32]. The similarity function is expected to be optimal, if the mirrored image is reflected at the true symmetry axis or plane, respectively. This procedure can be viewed as an registration approach of the original and mirrored image [19]. Other approaches are based on covariance matrices, whose eigenspaces must be invariant, if the model is symmetric [21,30] or phase information based on Gabor wavelet [36]. All those methods for symmetry plane detection rely either on 2-D information or 3-D information, respectively and do not bridge the connection between a symmetric 3-D object and its stack of 2-D transmission images.

We show that the 3-D symmetry plane can be estimated robustly in the projection domain and evaluate the robustness in dependence of a tilt between the symmetry plane and the circular source trajectory. Symmetry planes are regularly used for the detection of malformations, that are detectable as symmetry breakers within the human body, e.g. for tumor detection or in perfusion imaging [8,17]. Therefore, the symmetry plane estimation must be robust to outliers. We show the behavior of our algorithm in the presence of symmetry breakers.

Secondly we investigate the applicability of the symmetry prior for rigid motion estimation. Similar to state-of-the-art symmetry plane detection algorithm, a first category of motion estimation frameworks follow an approach based on registration. *Digitally rendered radiographs* (DRR) of an 3-D reconstruction — either obtained from an prior scan or as an motion affected intermediate reconstruction — are registered to the acquired projections based on a similarity metric [22, 3,7,31]. The motion trajectory is then found as the minimizer for the similarity metric. This approach can be optimized by placing radio-oblique markers on the object, however, at the cost of low contrast resolution and a cumbersome workload for the clinicians [4].

The second category optimizes an image quality metric (IQM) based on the reconstruction [16,28,34]. In an autofocus framework, the motion trajectory is found iteratively by optimizing for the IQM, e.g. entropy or total variation [34].

The third category, where our approach is classified, is based on enforcing cone-beam consistency [12,5]. We investigate how the symmetry prior can be utilized to estimate rigid patient motion using cone-beam consistency conditions and show that incorporating the symmetry prior in *epipolar consistency* (EC) outperforms *conventional epipolar consistency* (CEC) for in-plane motion estimation.

2 Methodology

2.1 Epipolar Consistency Conditions

Theory: An object acquired from two views reveals redundant low frequency information in both views. This property is well observable from the Fourier slice theorem, where each cone beam projection samples a cone in the 3-D Fourier space with the bottleneck incident to the origin. Grangeat's theorem describes a measure for redundancy based on the comparison of epipolar lines.

The theorem describes a transformation of epipolar lines to a value that is equal to the derivative of the 3-D radon value w.r.t. the radon plane normal — incident to corresponding epipolar plane — $\frac{\partial}{\partial d}\mathcal{R}f(\mathbf{n},d)$, where $\mathbf{n}$ is the plane normal and d denotes the plane offset. The transformation is a weighted integration along the epipolar line direction followed by a derivative [6,2] and successive weighting. We denote the transformation of an epipolar line on projection λ as intermediate value $S_\lambda(\mathbf{n})$ being defined by

$$S_\lambda(\mathbf{n}) = \int_{\mathcal{S}^2} \delta'(\mathbf{x}^\top\mathbf{n}) g_\lambda(\mathbf{x})\mathrm{d}\mathbf{x} = \frac{\partial}{\partial d}\mathcal{R}f(\mathbf{n},d)|_{d=\mathbf{c}_\lambda^\top\mathbf{n}} \ , \tag{1}$$

where $\delta'(\cdot)$ describes the derivative of the Dirac delta distribution, $g_\lambda(\mathbf{x})$ describes a single value on the detector, $\mathbf{c}_\lambda$ is the source position and $\mathbf{x}$ a vector from the source to a detector pixel.

Any two source positions share a bundle of epipolar lines. As a consequence of Eq. (1) any two corresponding epipolar lines share the same intermediate value. Thus, a perfectly consistent scan must fulfill that

$$S_a(\mathbf{n}) = S_b(\mathbf{n}) \qquad \forall\mathbf{n}\in\mathcal{S}^2 : \mathbf{c}_b^\top\mathbf{n} = \mathbf{c}_a^\top\mathbf{n} \ . \tag{2}$$

Any inconsistencies violate Eq. (2) and in turn, the consistency of a scan can be estimated by the distance of all corresponding intermediate values. To compare them, we need a sampling strategy and an appropriate distance measure.

Sampling Strategy: The intermediate values of a single projection can be precomputed as a look-up-table (LUT) from the cosine weighted projection data $\tilde{g}_\lambda$ as

$$S_\lambda(s,\vartheta) = \frac{s^2+D^2}{D^2}\ \frac{\partial}{\partial s}\mathcal{R}\tilde{g}_\lambda(s,\vartheta) \ , \tag{3}$$

where s and ϑ describe the offset and angle of line parameterizing the 2-D radon transform and D describes the source-detector-distance. The sampling strategy

then identifies the corresponding points in the LUT, referring the corresponding epipolar lines, that must match given the geometry information. We use projection matrices to describe the intrinsic and extrinsic parameters of a projection $\mathbf{P}_\lambda \in \mathbb{R}^{3\times4}$. The epipolar lines can be constructed by a pair of projection matrices $\mathbf{P}_a, \mathbf{P}_b$. In a first step, a line connecting the two source positions is found. Around this line, a plane parameterized by an angle ν is rotated. Due to the construction each rotated plane represents an epipolar plane and the respective epipolar lines on each detector are obtained by the projection of the epipolar plane on the detector [24]. As a result, for each detector we obtain the offset and angle of an epipolar line, which can be mapped to the respective s and ϑ values of the LUT. We denote this mapping as $s^{\nu}_{\mathbf{P}_a\mathbf{P}_b}$ and $\vartheta^{\nu}_{\mathbf{P}_a\mathbf{P}_b}$. This describes the s and ϑ values of the epipolar line on detector a corresponding to the epipolar plane parameterized by ν. The respective epipolar line on detector b is described by the mapping $s^{\nu}_{\mathbf{P}_b\mathbf{P}_a}$ and $\vartheta^{\nu}_{\mathbf{P}_b\mathbf{P}_a}$. A bundle of epipolar lines will then sample a line on the LUT. The whole process from two projection images to sampled consistency values is depicted in Fig. 1.

Distance Measure: The sampling process gives us two lines profiles, sampled from the LUT (cf. right plot of Fig. 1). Ideally these profiles would be identical and imaging defects, such as motion, beam hardening or scatter [35, 14, 1] are identifiable by unmatching line profiles. As the consistency measure is sensitive to any form of physical deviation from an idealized monochromatic X-ray transform [25], we use a weighted version of the robust German-McClure distance measure introducing a cutoff value σ, that we set empirically to 0.25. Based on Eq. (4) we define

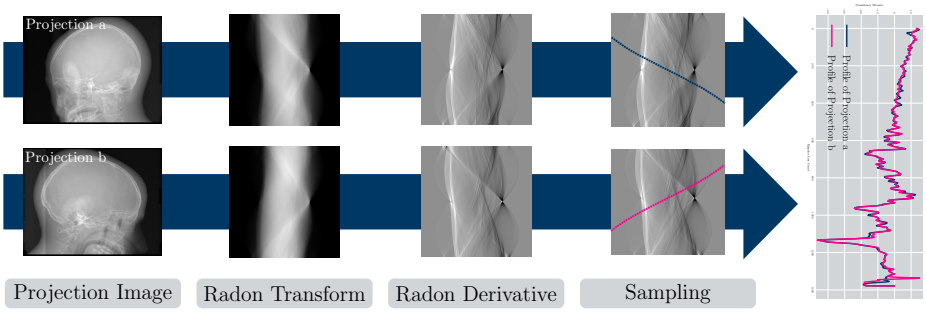

Fig. 1: Flowchart describing the generation of the LUT to pre-compute the intermediate values and the corresponding sampling scheme (weightings are omitted). First, the radon transform of a projection image is computed. Then, the radon image is differentiated in horizontal (s) direction using central differences. With the geometry information contained in $\mathbf{P}_a, \mathbf{P}_b$ the respective consistency values are sampled. The profiles sampled from the respective projections can be compared to calculate the consistency. Note that for motion compensation, only the sampling process changes as the geometry — i.e. the projection matrices — is modulated while the LUT remains static.

our consistency measure as

$$\mathrm{ECC}(\mathbf{P}_a, \mathbf{P}_b) = \sum_{\nu} \frac{(S_a(s^{\nu}_{\mathbf{P}_a\mathbf{P}_b}, \vartheta^{\nu}_{\mathbf{P}_a\mathbf{P}_b}) - S_b(s^{\nu}_{\mathbf{P}_b\mathbf{P}_a}, \vartheta^{\nu}_{\mathbf{P}_b\mathbf{P}_a}))^2}{1 + \frac{1}{\sigma}(S_a(s^{\nu}_{\mathbf{P}_a\mathbf{P}_b}, \vartheta^{\nu}_{\mathbf{P}_a\mathbf{P}_b}) - S_b(s^{\nu}_{\mathbf{P}_b\mathbf{P}_a}, \vartheta^{\nu}_{\mathbf{P}_b\mathbf{P}_a}))^2} \quad . \tag{4}$$

Any isometric transformation — e.g. direct isometries as rigid transformations or opposite isometries as reflections — can be incorporated in the projection matrices by a right-multiplication of the respective transformation matrix. This can be utilized to find a projection-wise rigid transformation that minimizes the inconsistency to estimate rigid patient motion [23, 12].

In-plane and Out-plane Parameters for Motion Estimation: A common strategy to estimate the patient motion is by minimizing Eq. (4) for all projection matrices of the acquired scan. Therefore, the estimated patient motion is described by a series of isometric translations $\mathbf{T} = [\mathbf{T}_1, \dots \mathbf{T}_N]$ where N is the number of acquired projections. This allows to define a motion state $\mathbf{T}_\lambda$ for each projection $\mathbf{P}_\lambda$ with $\mathbf{T}_\lambda$ incorporating the rotation around the three coordinate axes r_x, r_y, r_z and the translation along them t_x, t_y, t_z.

EC utilizes line integrals along epipolar lines to evaluate the consistency of two projections. Due to this integration, motion in the direction of epipolar lines is not detectable by this measure, as an integral over functions with compact support is shift invariant if the integration range is sufficient. As a consequence, motion estimation is split in two parameter categories: in-plane and out-plane parameters. In-plane parameters are motion directions within the plane of acquisition and out-plane parameters refer to the motions stepping out of the acquisition plane. State of the art short scan CBCT imaging protocols acquire 496 projections along an arc with a 200° coverage. Typically the t_z axis defines the normal of the acquisition plane incident to the acquired arc. Thus, the in-plane motion parameters are t_x, t_y, r_z and the out-plane motion parameters t_z, r_x, r_y. With the epipolar lines being mostly horizontal in a circular trajectory, in-plane motion is in the direction of epipolar lines. Consequently, in-plane motion is poorly estimated. In contrast, out-plane motion is well detectable [23] as such movement is mostly horizontal to the epipolar lines. By utilizing the symmetry prior, this categorization in out-plane and in-plane parameters can be broken by introducing X-shaped epipolar lines.

2.2 Symmetric View Augmentation

Given a photograph of a plane symmetric object, one can find a second view of that object revealing the same image, flipped at the vertical axis. Alternatively, a single photograph can be assigned to be acquired from two distinct views. This property extends to transmission imaging and allows the assignment of two projection matrices to one acquired image.

Symmetry in Transmission Imaging: We use the projective space $\mathbb{P}$ for the following calculations. The projective space allows for a compact definition of geometric transformations solely based on matrix multiplications and is commonly used for the definition of projection matrices [13, 29, 26]. The projective space $\mathbb{P}^n$ can be thought as an extension of the Euclidean space $\mathbb{R}^n$ by a hyperplane at infinity. For

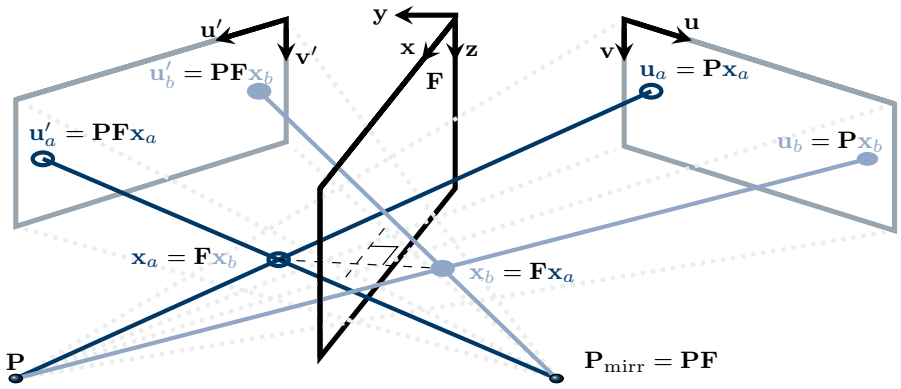

Fig. 2: Visualization of a plane symmetric scene.

the case $n = 3$ this would be a plane at infinity. This is achieved by introducing an additional homogeneous coordinate w. Points at infinity are then described by $w = 0$. Other than points at infinity, a point defined in $\mathbb{P}^n$ can be mapped to its Euclidean counterpart in $\mathbb{R}^n$ by removing the homogeneous component, and dividing all remaining coordinates by w.

Two points $\mathbf{x}_a \in \mathbb{P}^3$ and $\mathbf{x}_b \in \mathbb{P}^3$ reveal a plane symmetry if they can be mapped to each other by an involutive isometric transformation $\mathbf{F}$. Given a simple scene as depicted in Fig. 2 where the symmetry plane is incident to the $\mathbf{x} - \mathbf{z}$ axis, the transformation matrix only flips the sign of the y component of $\mathbf{x}_a$ or $\mathbf{x}_b$, respectively. They are related by $\mathbf{x}_a = \mathbf{F}\,\mathbf{x}_b$ and $\mathbf{x}_b = \mathbf{F}\,\mathbf{x}_a$. We see that the application of $\mathbf{F}$ twice results in the identity $\mathbf{FF} = \mathbf{1}$.

The projection $\mathbf{u}_a$ and $\mathbf{u}_b$ of $\mathbf{x}_a$ and $\mathbf{x}_b$ is found by $\mathbf{u}_a = \mathbf{P}\mathbf{x}_a$ and $\mathbf{u}_b = \mathbf{P}\mathbf{x}_b$. If we mirror the scene, we will project $\mathbf{F}\mathbf{x}_b$ and $\mathbf{F}\mathbf{x}_a$ instead of $\mathbf{x}_a$ and $\mathbf{x}_b$ which directly gives us the transformed projection geometry as

$$\mathbf{P}_{\text{mirr}} = \mathbf{PF} \ , \tag{5}$$

resulting in $\mathbf{u}'_a = \mathbf{PF}\mathbf{x}_a$ and $\mathbf{u}'_b = \mathbf{PF}\mathbf{x}_b$. Note, that from a calculus point of view, it does not matter whether we shift the scene, or the projection geometry. With $\mathbf{F}\mathbf{x}_a = \mathbf{x}_b$ and $\mathbf{F}\mathbf{x}_b = \mathbf{x}_a$ the resulting projection image will be identical, or stated inversely: one projection image can be assumed to be acquired with $\mathbf{P}$ or $\mathbf{P}_{\text{mirr}}$.

To estimate a symmetry plane, located arbitrarily in space, we need to find the transformation operation for the involutive mapping. Assume two plane symmetric points $\mathbf{x}'_a$ and $\mathbf{x}'_b$, that are the transformed points $\mathbf{x}_a$ and $\mathbf{x}_b$ under the isometric mapping $\mathbf{T}$, given as

$$\mathbf{x}'_a = \mathbf{T}\mathbf{x}_a \Leftrightarrow \mathbf{x}_a = \mathbf{T}^{-1}\mathbf{x}'_a \qquad \mathbf{x}'_b = \mathbf{T}\mathbf{x}_b \Leftrightarrow \mathbf{x}_b = \mathbf{T}^{-1}\mathbf{x}'_b \ . \tag{6}$$

They are connected by $\mathbf{x}'_b = \mathbf{F}'\mathbf{x}'_a$, with $\mathbf{F}'$ being the transformed involutive mapping we seek to derive. Utilizing the fundamental relationship of symmetry $\mathbf{F}\mathbf{x}_a = \mathbf{x}_b$ and replacing $\mathbf{x}_a$ and $\mathbf{x}_b$ using Eq. (6) gives

$$\mathbf{F}\mathbf{T}^{-1}\mathbf{x}'_a = \mathbf{T}^{-1}\mathbf{x}'_b \longrightarrow \mathbf{x}'_b = \mathbf{T}\mathbf{F}\mathbf{T}^{-1}\mathbf{x}'_a \ , \tag{7}$$

from which we can conclude the transformation rule given as

$$\mathbf{F}' = \mathbf{T}\mathbf{F}\mathbf{T}^{-1} \ . \tag{8}$$

Since we are basically transforming a plane incident to the $\mathbf{x}-\mathbf{z}$ plane, we can further restrict the isometric mapping $\mathbf{T}$ to three degrees of freedom, a rotation around the $\mathbf{z}$ axis α followed by a rotation around the $\mathbf{x}$ axis β and an offset in the normal direction of the plane d. This gives a general formulation of the involution defined by

$$\begin{aligned}\mathbf{F}(\alpha,\beta,d) \ = \ \mathbf{T}_{\alpha,\beta,d}\,\mathbf{F}\,\mathbf{T}^{-1}_{\alpha,\beta,d} = \\ \begin{pmatrix} \cos\alpha & -\sin\alpha\cos\beta & \sin\alpha\sin\beta & d\sin\alpha\cos\beta \\ \sin\alpha & \cos\alpha\cos\beta & -\sin\beta\cos\alpha & d\cos\alpha\cos\beta \\ 0 & \sin\beta & \cos\beta & d-\sin\beta \\ 0 & 0 & 1 & 1 \end{pmatrix} \begin{pmatrix} 1 & 0 & 0 & 0 \\ 0 & -1 & 0 & 0 \\ 0 & 0 & 1 & 0 \\ 0 & 0 & 0 & 1 \end{pmatrix} \\ \begin{pmatrix} \cos\beta & \sin\alpha & 0 & -d\sin\alpha \\ -\sin\alpha\cos\beta & \cos\alpha\cos\beta & \sin\beta & -d\cos\alpha\cos\beta \\ \sin\alpha\cos\beta & -\sin\beta\cos\alpha & \cos\beta & d\sin\beta\cos\alpha \\ 0 & 0 & 0 & 1 \end{pmatrix} \ .\end{aligned} \tag{9}$$

Symmetry Plane Estimation: The consistency measure is computed from a pair of projection matrices and the projection raw data (cf. Sec. 2.1). As we showed in the previous paragraph, the key concept is the assignment of a second mirrored geometry to each projection. Therefore, we can use EC (cf. Eq. (4)) to find an involutive transformation of the projections, representing the most consistent mapping

$$\sum_{a,b=1}^{N} \mathrm{ECC}(\mathbf{P}_a\mathbf{F}(\alpha,\beta,d),\mathbf{P}_b) \ , \tag{10}$$

which is by definition the reflection at the symmetry plane. This is achieved by minimizing Eq. (10), assuming that within each pair of projection $a, b \in N$ projection a is mirrored. Note that the LUT remains the same. The plane parameters α, β and d are found as the solution of the consistency minimization problem

$$(\hat{\alpha},\hat{\beta},\hat{d})^\top = \arg\min_{(\alpha,\beta,d)^\top} \sum_{a,b=1}^{N} \mathrm{ECC}(\mathbf{P}_a\mathbf{F}(\alpha,\beta,d),\mathbf{P}_b) \ . \tag{11}$$

The X-Trajectory: An inherent challenge for EC for short scans are the horizontal epipolar lines and the resulting splitting in out-plane directions, that are well detectable, and in-plane directions, that are not detectable robustly. The X-trajectory in the combination with the symmetry prior overcomes this challenge. The X-trajectory can be acquired with a conventional CBCT system by placing the symmetric object such that the symmetry plane is oblique to the trajectory plane as visualized in Fig. 3. We denote the tilt of the symmetry plane κ, and with an adequate κ the epipolar lines will form an X-shaped pattern due to the dual geometric interpretability of each projection. If the tilt is great enough such that the whole object can be placed below the first and above the last projection while not being truncated axially, the scan will be data complete as it fulfills Tuy's condition.

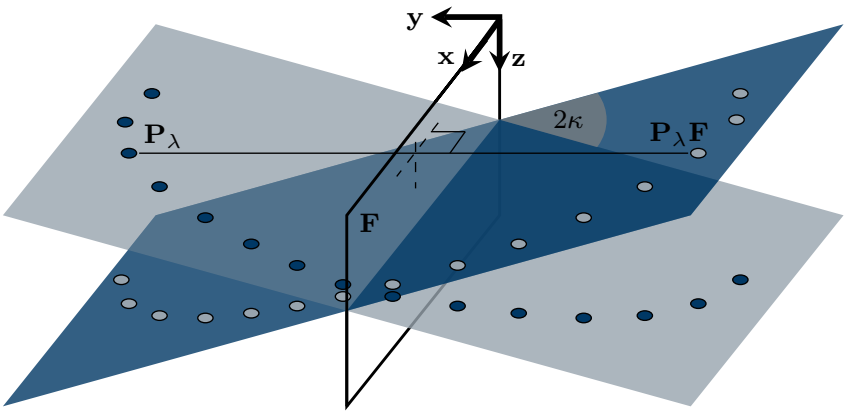

Fig. 3: Visualization of the X-trajectory with tilt angle κ. The acquired trajectory is embedded in the blue trajectory plane (gray dots) and the mirrored virtual trajectory is embedded in the gray trajectory plane (blue dots).

3 Experiments

3.1 Datasets

We acquired short scans of two anthropomorphic human head phantoms on a robotic C-arm system (Artis zeego, Siemens Healthcare GmbH, Germany). The first phantom is denoted as phantom A, and the second as phantom B. We further processed phantom A, such that it is perfectly symmetric. To this end, we first performed a reconstruction and then symmetrized the volume. In a second step we simulate DRRs of the symmetrized head phantom using CONRAD [18]. As a consequence, we know the ground truth symmetry plane of the phantom. A reconstruction of the aligned symmetrized phantom A is depicted in Fig. 4a and four DRRs are shown in Fig. 4b. We generated DRRs of the symmetrized phantom A with five tilt angles: $0°, 10°, 20°, 30°$ and $45°$.

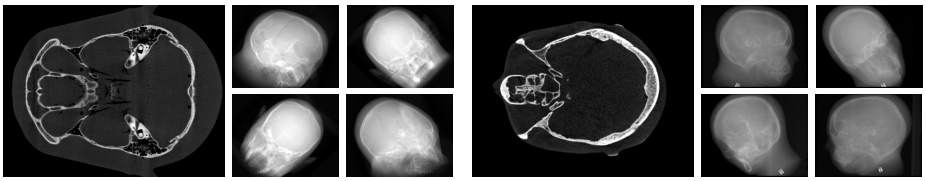

(a) (b) (c) (d)

Fig. 4: Visualization of acquired datasets. (a): Slice through the symmetrized phantom A, (b): digitally rendered radiographs (DRR) of the symmetrized phantom A, (c): aligned reconstruction of anthropomorphic head phantom B, (d): raw projection data from a short scan of the anthropomorphic head phantom B.

To further validate the presented method on real data — inherently incorporating physical artifacts — we use the raw projection data from phantom B. As expected in a real clinical scenario, the head phantom does not exhibit a perfect plane symmetry. The dataset was acquired three times with varying positioning on the scanner. We arrange the phantom such that different tilt angles of the symmetry plane and the trajectory plane are achieved. An aligned reconstruction slice of phantom B is given in Fig. 4c and raw projections from the scan revealing a tilt angle are depicted in Fig. 4d.

3.2 Estimation of Symmetry Plane

Equation (10) defines the consistency of a scan w.r.t. the symmetry plane parameters β, α and d based on the projection raw data only. We find the symmetry plane, by solving the optimizing problem defined by Eq. (11) using the Nelder-Mead method. The optimization is initialized based on the anterior-to-posterior projection (e.g. as depicted in the upper right of Fig. 4b). The relative position of this projection is used to initialize α (in our experiments always $90°$), whereas the approximate tilt of the head initializes β. The offset parameter is initialized to be $d = 0$. The estimated symmetry plane parameters for dataset B are displayed in Tab. 1. Since we have created the symmetry of dataset A synthetically we do not need to estimate it beforehand.

Symmetry Plane Computation as a Function of Tilt Angle: We inspect the behavior of our cost function near the optimum solution in dependence of the tilt angle κ. For the real projection data, we use the plane parameters estimated using the Nelder-Mead method (cf. Tab. 1) as optimal plane parameters and for the symmetrized head phantom we use the respective ground truth plane parameters. By construction we choose them to be $\beta = 0, \alpha = 0, d = 0$. Instead of moving the dataset, we use a rotated trajectory to generate the desired tilt angles.

Starting from the optimal solution we then modulate a single plane parameter, while keeping the other two parameters fixed. For each modulation we evaluate the consistency defined by Eq. (10).

Outlier Robustness of Symmetry Plane Estimation In a real clinical environment, symmetry breakers are common. The patient might suffer from lateral stroke or tumors. Further, dental implants or surgical tools can be present. This experiment inspects the robustness of the symmetry plane w.r.t. locally restricted symmetry breakers. As we only want to inspect the sole dependence on the symmetry breakers we use a symmetrized version of phantom B. To this end, we reconstruct the dataset with the FDK algorithm and mirror the reconstruction at the estimated symmetry plane (cf. Tab. 1). We use the clinically most relevant case with $\kappa \approx 2°$. In a second step we place a 3-D ellipse in the reconstruction, simulating a specific symmetry breaker. We simulated a hemorrhagic stroke, a dental implant and two surgical tools. The surgical tools only differ in the HU offsets. The ellipse volume, together with the applied HU offset is documented in Tab. 2 and a slice of the reconstructed volume showing the respective symmetry breaker is depicted in Fig. 5.

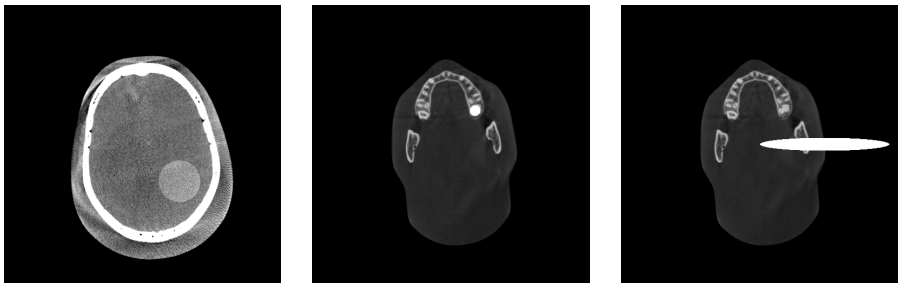

Fig. 5: Reconstruction slices of symmetrized phantom B with induced symmetry breakers. Left: lateral hemorrhagic stroke with 90 HU offset (HU [800-1300]), middle: dental implant with 2000 HU offset (HU [500-3700]), right: surgical tool with 12000 HU offset (HU [800-1300]).

3.3 Application to Rigid Motion

With *conventional epipolar consistency* (CEC) [12,24,25,2] inherent limitations reduce the robustness of in-plane motion estimation (cf. Sec. 2.1) due to the formation of mostly horizontal epipolar lines. Based on Eq. (4) the CEC of two views is defined as

$$\mathrm{CEC}(\mathbf{P}_a\mathbf{T}_a, \mathbf{P}_b\mathbf{T}_b) := \mathrm{ECC}(\mathbf{P}_a\mathbf{T}_a, \mathbf{P}_b\mathbf{T}_b) \ , \tag{12}$$

with $\mathbf{T}_\lambda$ denoting the motion state of projection $\mathbf{P}_\lambda$ as introduced in Sec. 2.1.

Utilizing the X-trajectory with adequate tilt κ we achieve X-shaped epipolar lines allowing a more robust estimation of in-plane parameters. We denote the consistency incorporating the symmetry plane *mirrored epipolar consistency* (MEC) being defined by

$$\mathrm{MEC}(\mathbf{P}_a\mathbf{F}(\alpha,\beta,d)\mathbf{T}_a, \mathbf{P}_b\mathbf{T}_b) := \mathrm{ECC}(\mathbf{P}_a\mathbf{F}(\alpha,\beta,d)\mathbf{T}_a, \mathbf{P}_b\mathbf{T}_b) \ . \tag{13}$$

To validate the impact of the symmetry prior we perform a motion analysis using the acquired projection data of the anthropomorphic human head phantom (phantom B). To inspect the dependency of the tilt, we used the scans acquired with a tilt angle $\kappa \approx 2^\circ$ and $\kappa \approx 37^\circ$. We use the symmetry plane, as estimated by the Nelder-Mead method (cf. Tab. 1). For each motion direction of the motion vector $\mathbf{m}^\lambda = (t_x^\lambda, t_y^\lambda, t_z^\lambda, r_x^\lambda, r_y^\lambda, r_z^\lambda)$ we optimize one projection, while keeping all others fixed. This is performed using MEC and CEC, respectively. Thus, for each motion direction m_k^λ with $k \in \{1, 2 \cdots 6\}$ and each projection λ of the trajectory we evaluate

$$\hat{m}_k^\lambda = \arg\min_{m_k^\lambda} \sum_{a,b=1}^{N} \mathrm{CEC}(\mathbf{P}_a\mathbf{T}_a(m_k^a), \mathbf{P}_b\mathbf{T}_b(m_k^b)) \tag{14}$$

$$\hat{m}_k^\lambda = \arg\min_{m_k^\lambda} \sum_{a,b=1}^{N} \mathrm{MEC}(\mathbf{P}_a\mathbf{F}(\alpha,\beta,d)\mathbf{T}_a(m_k^a), \mathbf{P}_b\mathbf{T}_b(m_k^b)) \quad , \tag{15}$$

with $\mathbf{T}_\lambda(m_k^\lambda)$ being the transformation matrix, performing a transformation of projection $\mathbf{P}_\lambda$ by m_k^λ. Note that in Eq. (14) and Eq. (15) all $\mathbf{T}_i(m_k^i)$ with $i \neq \lambda$

Table 1: Estimated symmetry plane parameters for the three acquired short scans of phantom B. In the text, we refer to the respective scan using the approximate tilt angle 2°, 22° and 37°, respectively.

Dataset	Tilt Angle κ [°]	β [°]	α [°]	d [mm]
B	$2.4938 \approx 2$	2.4938	84.5757	3.9529
B	$22.2612 \approx 22$	22.2612	81.3196	6.7057
B	$37.3278 \approx 37$	37.3278	83.0196	6.6659

are the identity. This gives for CEC and MEC, respectively a line profile for each motion direction, dataset and tilt angle κ which are depicted in Fig. 8 and Fig. 9. The x-axis of the line profile is the projection number λ and the y-axis denotes the deviation from the ground truth m_k^λ, either defined by CEC or MEC. Note that we optimize the consistency on a motion free trajectory. Therefore, an ideal motion measure would not alter the trajectory. However, by inspecting the behavior on a motion free trajectory we obtain a good insight on the expected precision.

4 Results and Discussion

4.1 Estimation of Symmetry Plane

Symmetry Plane as a Function of Tilt Angle: The symmetry plane estimation near the optimum is shown in Fig. 6 for the synthetic data (Phantom A) and in Fig. 7 for the real data (Phantom B). Each figure consists of three subplots, with the upper plot showing the results for the offset parameter d, the middle plot showing the β results and the bottom plot depicts the results for the α parameters. Both, the synthetic and real data, show that the symmetry plane is well defined using the applied consistency measure independent of the tilt angle. However, with a steeper tilt angle, the minimum of the offset parameter is much sharper and in the consequence more stable. For the real data, a steeper tilt angle also results in sharper minima for the β and α parameters.

Near a β offset of $-25°$ the phantom reveals a light symmetry, resulting in a local minimum. Such local minima and maxima provide information about the capture range, e.g. β must be initialized within a range of $\approx \pm 12°$ deviation from the ground truth, whereas d has a high capture range of $\approx \pm 50$ mm.

Outlier Robustness of Symmetry Plane Estimation: The estimated symmetry plane parameters with simulated symmetry-breakers are listed in Tab. 2 together with a reference estimation, giving the ground truth. The stronger the symmetry breaker, the more inconsistency is induced. However, due to the robust norm, the consistency differences of the surgical tool with 6000 and 12000 HU differences induce a similar inconsistency. The symmetry plane estimation is merely affected by the symmetry breakers. In all cases the estimated parameters reveal a maximum error of 0.16° and less then 0.04 mm.

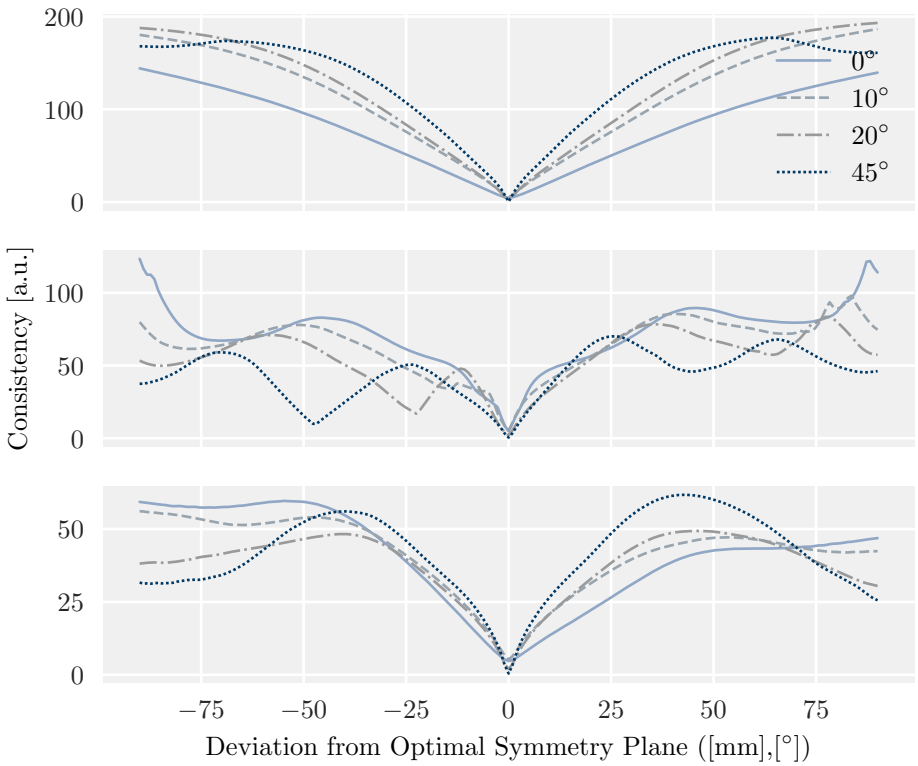

Fig. 6: Obtained consistency w.r.t. a deviation from the optimal symmetry plane parameter and tilt angle κ using the symmetrized phantom A. Top: consistency dependent on deviation by an offset d from optimum. Middle: consistency dependent on a β rotation. Bottom: consistency dependent on a α rotation.

Table 2: Estimated symmetry plane parameters in the presence of outliers.

Symmetry Breaker	HU Diff. [HU]	Vol. [mm^3]	β [°]	α [°]	d [mm]	EC [a.u.]
None	0	0	2.4151	84.7220	3.9805	30.7520
Stroke	90	282.74	2.4576	84.5661	3.9421	36.9024
Dental Implant	2000	70.69	2.4846	84.5805	3.9481	73.8048
Surgical Tool	6000	2827.43	2.4891	84.5748	3.9532	84.8755
Surgical Tool	12000	2827.43	2.4869	84.6026	3.9641	86.1056

4.2 Application to Rigid Motion

We cluster the results of the experiments as explained in Sec. 3.3 for out-plane motions (cf. Fig. 9) and in-plane motions (cf. Fig. 8). Note that in our experiment for every projection λ the consistency is optimized by changing a single motion parameter only affecting the projection number λ. Each optimization is initialized with the motion free trajectory, therefore the deviation in projection $\lambda = i$ is independent on the deviation in projection $\lambda = j$ $(i \neq j)$. As expected and previ-

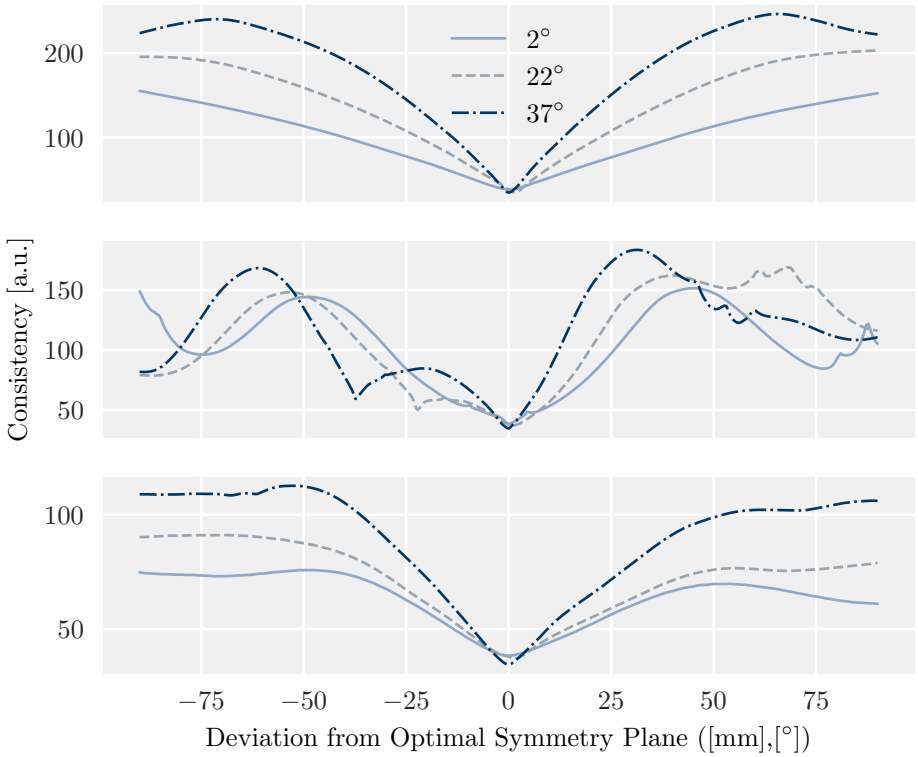

Fig. 7: Obtained consistency w.r.t. a deviation from the optimal symmetry plane parameter and tilt angle κ using the real projection raw data of phantom B. Top: consistency dependent on deviation by an offset d from optimum. Middle: consistency dependent on a β rotation. Bottom: consistency dependent on a α rotation.

ously reported in [12, 24], the in-plane motions are not robustly estimated by CEC, whereas the out-plane motion is much more accurate. In contrast, the proposed method is more accurate in most areas then CEC if an sufficient tilt angle κ is chosen (cf. Fig. 8). However, MEC reveals a high deviation from the ground truth in the mid trajectory, where the central ray of the projections is almost parallel to the symmetry plane. We expect, that in these areas the mirroring of projections is ill conditioned, especially in the presence of an imperfect symmetry.

For the out-plane parameters the CEC is already accurate and the proposed method has only few segments where it slightly performs better the CEC. The MEC reveals again an offset at the projections near the symmetry plane. Especially for the t_z translation, the CEC is more accurate. In general our proposed MEC outperforms CEC on the in-plane parameters, whereas CEC is superior for out-plane parameters.

Numeric evaluations of the curves are documented in Tab. 3. Note that the presented values are an average over the whole trajectory and only provide a rough impression. MEC is strongly view dependent, and displays high inaccuracies near

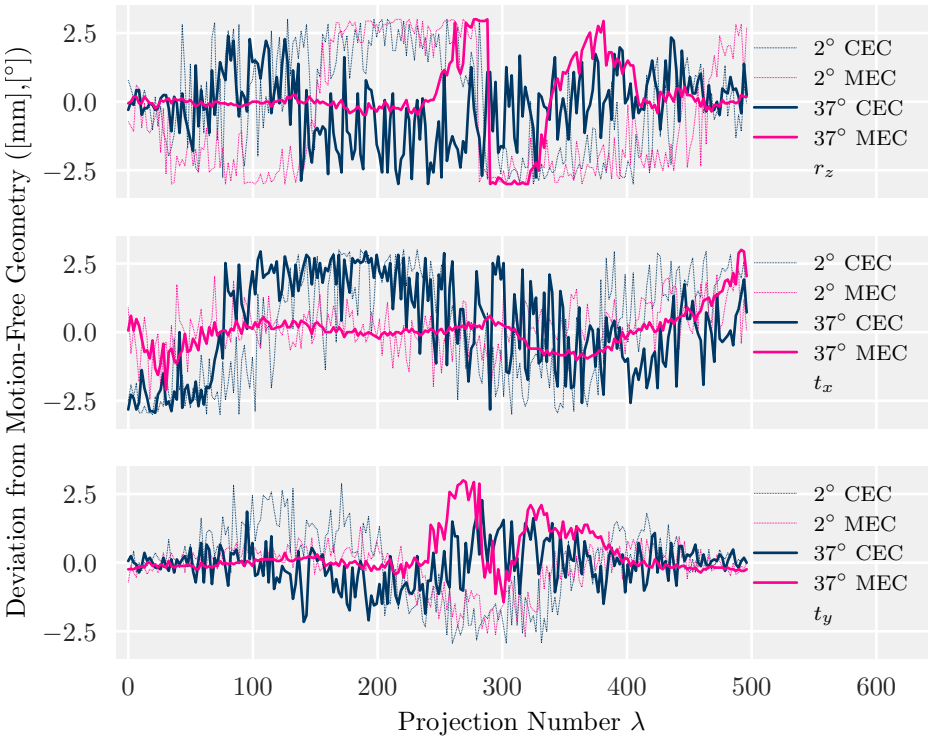

Fig. 8: Motion analysis for in-plane parameters. Each subplot shows the performance of the proposed method (MEC) and the conventional EC (CEC) with a tilt angle $\kappa = 2°$ and $\kappa = 37°$, respectively. Top: in dependence of r_x, mid: in dependence of r_y, bottom: in dependence of t_z.

the symmetry plane, while being accurate in the first part of the trajectory. This behavior is not captured by the mean or standard deviation. However, Tab. 3 supports our visual inspection, that out-plane parameters are already well estimated by CEC, and the in-plane estimation is improved by MEC, given a tilt angle $\kappa = 37°$.

Another interesting result is the strong object dependency of the CEC. To our knowledge, this behavior was not reported in the literature so far. It is observable in all plots, that the CEC behaves differently depending on the placement of the phantom in the scanner, i.e. the tilt angle κ, also the numeric results clearly show a significant change.

5 Conclusion and Outlook

We have presented the powerful concept of symmetry for transmission imaging in combination with EC. By estimating the symmetry plane in the projection domain our method is fast and independent of a fully sampled scan. A single

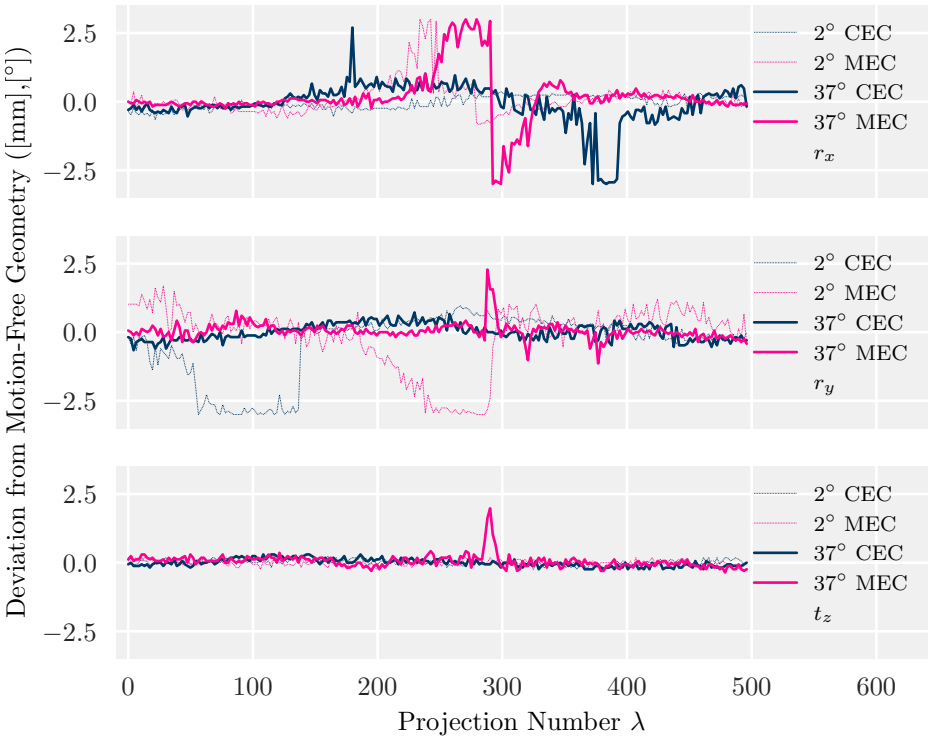

Fig. 9: Motion analysis for out-plane parameters. Each subplot shows the performance of the proposed method (MEC) and the conventional EC (CEC) with a tilt angle $\kappa = 2°$ and $\kappa = 37°$, respectively. Top: in dependence of r_x, mid: in dependence of r_y, bottom: in dependence of t_z.

kernel call, evaluating once Eq. (10), takes about 50 ms on a mobile computer with NVIDIA Quadro M2200. We have evaluated the proposed algorithm on a real scan of an anthropomorphic head phantom. Despite being only partially symmetric, the proposed concept of exploiting symmetry was still found applicable. On the anthropomorphic phantom, the symmetry plane can be estimated robustly and we have provided experiments allowing to conclude, that symmetry breakers merely affect the symmetry plane estimation. While the overall inconsistency increases proportional to the induced asymmetry, the minimum of the estimation does not change. This is of high relevance when the method should be applied e.g. for tumor or stroke detection, where symmetry breakers are used to identify abnormalities [8].

We further provided promising results for in-plane motion compensation. EC is known to be robust for out-plane motion detection (cf. Fig. 9), in-plane motion is challenging. We showed that the symmetry prior (MEC) outperforms CEC in most parts of the trajectory. A drawback of MEC is the location dependent performance. Especially in the part of the trajectory near the symmetry plane the motion estimation is inaccurate. As a consequence, highly sophisticated motion es-

Table 3: Numeric evaluation of motion analysis. The mean error is documented together with the mean value and standard deviation computed from each curve depicted in Fig. 8 and Fig. 9. All values are in degree or mm, respectively.

Motion Direction	Consistency	κ=2° Mean error	κ=2° Mean	κ=2° Std. Dev.	κ=37° Mean error	κ=37° mean	κ=37° Std. Dev.
r_z	CEC	1.615	0.108	1.844	0.997	-0.186	1.246
r_z	MEC	2.156	-0.574	2.222	0.729	0.101	1.227
t_x	CEC	1.723	0.144	1.94	1.559	0.309	1.758
t_x	MEC	0.651	0.175	0.842	0.454	0.054	0.688
t_y	CEC	1.025	-0.025	1.313	0.592	-0.081	0.769
t_y	MEC	0.592	-0.21	0.8	0.487	0.293	0.789
r_x	CEC	0.219	-0.037	0.238	0.506	-0.087	0.758
r_x	MEC	0.357	0.097	0.609	0.482	0.173	0.922
r_y	CEC	0.788	-0.407	1.172	0.254	0.013	0.294
r_y	MEC	0.811	-0.146	1.156	0.18	0.046	0.307
t_z	CEC	0.08	0.014	0.103	0.111	-0.004	0.138
t_z	MEC	0.068	-0.001	0.088	0.155	0.051	0.245

timation strategies are necessary for the compensation, that only incorporate trajectory segments that are highly reliable. For our experiments we only inspected the symmetry prior. In a practical scenario, additional prior knowledge, e.g. a smooth motion trajectory, can be incorporated into the objective function. This constrained was shown to be highly beneficial by [28] in the context of autofocus, but would translate seamlessly to consistency based algorithms.

For our motion experiments, we assumed the symmetry plane to be known. This assumption might not hold in a clinical setting, especially in the presence of motion. However, we have experienced, that two views can be sufficient for the symmetry estimation using synthetic data. While the symmetry plane estimation on real data needs sufficient views to work properly, an alternating approach, that compensates for motion and finds the symmetry plane seems a promising solution.

We conclude that symmetry is a powerful concept in transmission imaging with the potential to benefit diverse imaging problems that make use of consistency condition such as, beam hardening- or truncation-correction. Beside motion compensation, the most promising application is expected in the context of calibration, where a calibration phantom with several symmetry planes could be used to achieve a view-independent calibration performance.

Disclaimer: The concepts and information presented in this paper are based on research and are not commercially available.

Conflict of interest: M. Unberath, J. Fotouhi, N. Navab and A. Maier have no conflict of interest. A. Preuhs and E. Hoppe are funded by Siemens Healthcare GmbH, Forchheim Germany. M. Kowarschik and M. Manhart are employees of Siemens Healthcare GmbH, Forchheim Germany.

Informed consent: This article does not contain patient data.

References

1. Abdurahman, S., Frysch, R., Bismark, R., Melnik, S., Beuing, O., Rose, G.: Beam hardening correction using cone beam consistency conditions. TMI **37**(10), 2266–2277 (2018)
2. Aichert, A., Berger, M., Wang, J., Maass, N., Doerfler, A., Hornegger, J., Maier, A.K.: Epipolar Consistency in Transmission Imaging. TMI **34**(11), 2205–2219 (2015)
3. Berger, M., Müller, K., Aichert, A., Unberath, M., Thies, J., Choi, J.H., Fahrig, R., Maier, A.: Marker-free motion correction in weight-bearing cone-beam CT of the knee joint. Med. Phys. **43**(3), 1235–1248 (2016)
4. Choi, J.H., Fahrig, R., Keil, A., Besier, T.F., Pal, S., McWalter, E.J., Beaupré, G.S., Maier, A.: Fiducial marker-based correction for involuntary motion in weight-bearing c-arm ct scanning of knees. part i. numerical model-based optimization. Med. Phys. **40**(9) (2013)
5. Debbeler, C., Maass, N., Dennerlein, F., Buzug, T.: A New CT Rawdata Redundancy Measure applied to Automated Misalignment Correction. Fully3D pp. 264–267 (2013)
6. Defrise, M., Clack, R.: A Cone-Beam Reconstruction Algorithm Using Shift-Variant Filtering and Cone-Beam Backprojection. TMI **13**(1), 186–195 (1994)
7. Dennerlein, F., Jerebko, A.: Geometric jitter compensation in cone-beam CT through registration of directly and indirectly filtered projections. IEEE Nuclear Science Symposium Conference Record (3), 2892–2895 (2012)
8. Erihov, M., Alpert, S., Kisilev, P., Hashoul, S.: A Cross Saliency Approach to Asymmetry-Based Tumor Detection. MICCAI **9351**, 636–643 (2015)
9. Field, M., Golubitsky, M.: Symmetry in chaos: a search for pattern in mathematics, art, and nature. SIAM (2009)
10. Francois, A.R., Medioni, G.G., Waupotitsch, R.: Reconstructing mirror symmetric scenes from a single view using 2 view stereo geometry. ICPR pp. 12–16 (2002)
11. Francois, A.R., Medioni, G.G., Waupotitsch, R.: Mirror symmetry 2 - view stereo geometry. Image and Vision Computing **21**(2), 137–143 (2003)
12. Frysch, R., Rose, G.: Rigid motion compensation in C-arm CT using consistency measure on projection data. MICCAI pp. 298–306 (2015)
13. Hartley, R., Zisserman, A.: Multiple view geometry in computer vision. Cambridge university press (2003)
14. Hoffmann, M., Würfl, T., Maaß, N., Dennerlein, F., Aichert, A., Maier, A.K.: Empirical scatter correction using the epipolar consistency condition. CT-Meeting (2018)
15. Khotanlou, H., Colliot, O., Atif, J., Bloch, I.: 3d brain tumor segmentation in mri using fuzzy classification, symmetry analysis and spatially constrained deformable models. Fuzzy sets and systems **160**(10), 1457–1473 (2009)
16. Kingston, A., Sakellariou, A., Varslot, T., Myers, G., Sheppard, A.: Reliable automatic alignment of tomographic projection data by passive auto-focus. Med. Phys. **38**(9), 4934–45 (2011)
17. Liu, S.X.: Symmetry and asymmetry analysis and its implications to computer-aided diagnosis: A review of the literature. J. Biomed. Inform. **42**(6), 1056 – 1064 (2009)
18. Maier, A., Hofmann, H., Berger, M., Fischer, P., Schwemmer, C., Wu, H., Müller, K., Hornegger, J., Choi, J.H., Riess, C., Keil, A., Fahrig, R.: CONRAD - A software framework for cone-beam imaging in radiology. Med. Phys. **40**(11), 111914 (2013)
19. Markelj, P., Tomaževič, D., Likar, B., Pernuš, F.: A review of 3D/2D registration methods for image-guided interventions. Medical Image Analysis **16**(3), 642–661 (2012)
20. Marola, G.: On the detection of the axes of symmetry of symmetric and almost symmetric planar images. IEEE Transactions on Pattern Analysis and Machine Intelligence **11**(1), 104–108 (1989)
21. O'Mara, D., Owens, R.: Measuring bilateral symmetry in digital images **1**, 151–156 (1996)
22. Ouadah, S., Jacobson, M., Stayman, J.W., Ehtiati, T., Weiss, C., Siewerdsen, J.H.: Correction of patient motion in cone-beam CT Correction of patient motion in cone-beam CT using 3D – 2D registration. Physics in Medicine & Biology (2017)
23. Preuhs, A., Maier, A., Manhart, M., Fotouhi, J., Navab, N., Unberath, M.: Double your views - exploiting symmetry in transmission imaging. MICCAI (2018)
24. Preuhs, A., Manhart, M., Maier, A.: Fast Epipolar Consistency without the Need for Pseudo Matrix Inverses. CT-Meeting pp. 202–205 (2018)
25. Preuhs, A., Nishant, R., Manhart, M., Maier, A.: Maximum likelihood estimation of head motion using epipolar consistency. BVM (2018)
26. Richter-Gebert, J.: Perspectives on projective geometry: A guided tour through real and complex geometry. Springer Science & Business Media (2011)

27. Rothwell, C., Forsyth, D.A., Zisserman, A., Mundy, J.L.: Extracting projective structure from single perspective views of 3d point sets. ICV pp. 573–582 (1993)
28. Sisniega, A., Stayman, J.W., Yorkston, J., Siewerdsen, J.H., Zbijewski, W.: Motion compensation in extremity cone-beam CT using a penalized image sharpness criterion. Physics in Medicine and Biology **62**(9), 3712–3734 (2017)
29. Stolfi, J.: Oriented projective geometry: A framework for geometric computations. Academic Press (2014)
30. Sun, C., Sherrah, J.: 3d symmetry detection using the extended gaussian image. IEEE transactions on pattern analysis and machine intelligence **19**(2), 164–168 (1997)
31. Sun, T., Kim, J.H., Fulton, R., Nuyts, J.: An iterative projection-based motion estimation and compensation scheme for head X-ray CT. Med. Phys. **43**(10), 12 (2016)
32. Tuzikov, A.V., Colliot, O., Bloch, I.: Brain symmetry plane computation in mr images using inertia axes and optimization. In: Object recognition supported by user interaction for service robots, vol. 1, pp. 516–519. IEEE (2002)
33. Vinhais, C., Campilho, A.: Optimal detection of symmetry axis in digital chest x-ray images. In: Iberian Conference on Pattern Recognition and Image Analysis, pp. 1082–1089. Springer (2003)
34. Wicklein, J., Kunze, H., Kalender, W.a., Kyriakou, Y.: Image features for misalignment correction in medical flat-detector CT. Med. Phys. **39**(8), 4918 (2012)
35. Würfl, T., Maaß, N., Dennerlein, F., Huang, X., Maier, A.K.: Epipolar consistency guided beam hardening reduction-ecc^2. Fully 3D (2017)
36. Xiao, Z., Hou, Z., Miao, C., Wang, J.: Using phase information for symmetry detection. Pattern recognition letters **26**(13), 1985–1994 (2005)